

Article

Intelligent Space Thermal Control Radiator Based on Phase Change Material with Partial Visible Transparency

Xianghao Kong ^{1,*}, Hezhi Sun ^{1,*}, Shiri Liang ², Zao Yi ^{3,*}, Naiting Gu ⁴ and Yougen Yi ⁵¹ China Academy of Space Technology, Beijing 100094, China; kongxianghao01@126.com² School of Physics and Optoelectronic Engineering, Yangtze University, Jingzhou 434023, China; 119947770715@163.com³ Joint Laboratory for Extreme Conditions Matter Properties, Southwest University of Science and Technology, Mianyang 621010, China⁴ Key Laboratory on Adaptive Optics, Institute of Optics and Electronics, Chinese Academy of Sciences, Chengdu 610209, China; gnt7328@163.com⁵ College of Physics, Central South University, Changsha 410083, China; yougenyi@csu.edu.cn

* Correspondence: sunhezhi@hotmail.com (H.S.); yizaomy@swust.edu.cn (Z.Y.)

Abstract: Coating structures with dynamically adjustable infrared emissivity are crucial in spacecraft components to cope with the transient thermal environments of space. For a long time, thermochromic phase change materials have been widely used in applications requiring emissivity adjustment, and optimizing the range of adjustable infrared emissivity has always been at the forefront of research. However, reducing the absorption of solar radiation has significant implications for the practical application and thermal stability of spacecraft components in space environments. In this paper, we propose a multilayer film structure based on the phase change material VO₂ combined with the materials ZnSe and ITO to achieve low solar radiation absorption and adjustable infrared emissivity for intelligent thermal radiators in space. Through finite element simulation analysis of the structure, we achieve a solar radiation absorption rate of 0.3 and an adjustable infrared emissivity of 0.49. According to Stefan–Boltzmann’s law, the structure exhibits strong radiative heat dissipation at high temperatures and weak energy dissipation at low temperatures to maintain the thermal stability of the device and ensure efficient operation. The intelligent thermal radiator operates based on the principles of Fabry–Perot resonance. Therefore, the multilayer structure based on the phase change material VO₂ demonstrates excellent performance in both solar radiation absorption and adjustable infrared emissivity, showcasing its tremendous potential in the field of intelligent thermal control in aerospace.

Keywords: infrared emissivity; thermal radiator; phase change material; Fabry–Perot

Citation: Kong, X.; Sun, H.; Liang, S.; Yi, Z.; Gu, N.; Yi, Y. Intelligent Space Thermal Control Radiator Based on Phase Change Material with Partial Visible Transparency. *Coatings* **2024**, *14*, 535. <https://doi.org/10.3390/coatings14050535>

Academic Editor: Dimitrios Tasis

Received: 21 March 2024

Revised: 15 April 2024

Accepted: 22 April 2024

Published: 25 April 2024



Copyright: © 2024 by the authors. Licensee MDPI, Basel, Switzerland. This article is an open access article distributed under the terms and conditions of the Creative Commons Attribution (CC BY) license (<https://creativecommons.org/licenses/by/4.0/>).

1. Introduction

Spacecraft components are constantly subjected to changes in environmental temperature due to the rotation of the sun, requiring thermal management to maintain long-term operation. Radiative heat transfer into outer space is an effective measure for thermal management, with thermal radiation playing a central role [1–6]. In space, spacecraft must efficiently dissipate heat to maintain an appropriate temperature for internal instruments and equipment. Traditional thermal radiators, however, cannot adaptively adjust the infrared radiation required due to temperature changes, making them unsuitable for the complex environments of space. To address this issue, variable emissivity thermal control coatings are typically added to assist in maintaining spacecraft within ideal temperature ranges. According to Stefan–Boltzmann’s law, when spacecraft components are in a higher temperature environment, coatings with higher emissivity structures can dissipate heat, while when spacecraft components are at a lower ambient temperature, the emissivity decreases to reduce radiative heat loss, thus maintaining a stable temperature [7].

Recently, researchers have paid more attention to spacecraft thermal control coatings, aiming to enhance their practical application value and propose designs more in line with needs. Specifically, the goal is to maintain infrared thermal control while minimizing the impact of solar radiation absorption on device performance [8,9]. The research on smart thermal control coatings typically involves the combination design of thermochromic phase change material with other materials to provide effective thermal radiation control. Concerning the need for low solar radiation absorption, phase change material can be designed in the form of metasurfaces to facilitate reducing solar absorptance, while exploiting surface plasmon effects to achieve adjustable infrared emission [10–14]. In this paper, we aim to improve the transparency of metasurface structures by selecting appropriate structural materials, thereby reducing solar absorptance and significantly demonstrating their infrared emission adjustability through the Fabry–Perot (FP) effect in a multilayer film structure. Among them, due to the characteristics of Vanadium dioxide (VO_2) material, applications have been extended to smart roof tiles and smart glass [15,16].

Materials for dynamic thermal management have gained rapid attention due to their ability to adapt to fluctuating environments and achieve higher energy efficiency compared to static modulation. Typically, phase change materials such as VO_2 can be used for adaptive and reversible processes [17–20]. At the critical phase transition temperature $T_c = 68\text{ }^\circ\text{C}$, the material undergoes a transition from a low-temperature semiconductor state to a high-temperature metallic state. VO_2 exhibits a monoclinic structure at low temperatures, while it exhibits a tetragonal structure at high temperatures. During the phase transition process, the emissivity of VO_2 also changes. Based on this characteristic, Kruzelecky et al. initially proposed depositing VO_2 films on metal substrates to achieve adjustable emissivity. The results indicate that the emissivity modulation is 0.22. Research has shown that when high-reflectivity metal substrates are configured under VO_2 films, the thermochromic properties of VO_2 can be utilized to further modulate emissivity [21]. Subsequently, researchers have proposed studies on enhancing the performance of spacecraft intelligent radiators based on VO_2 /metal multilayer film structures. Gu et al. addressed these issues by proposing an intelligent infrared radiation regulator based on the FP cavity structure ($\text{VO}_2/\text{HfO}_2/\text{Al}$), which achieved tunable infrared emissivity of 0.51 through high-power pulsed magnetron sputtering, and by doping with tungsten (W) to lower the phase transition temperature to near room temperature, $27.5\text{ }^\circ\text{C}$ [22]. Araki et al. conducted direct measurements on a solid-state passive switchable radiator utilizing VO_2 in simulated space conditions. A BaF_2 dielectric layer was added between the VO_2 layer and the Au reflection layer to achieve passive switchable thermal emission control based on the VO_2 phase transition [23]. These investigations suggest that FP resonators can significantly improve the emissivity modulation capabilities of intelligent thermal control devices for spacecraft. Therefore, designing FP resonators in the structure has inspiring significance for further research [24–26].

This paper presents an intelligent radiation device for spacecraft based on the phase change material VO_2 , which achieves low solar radiation absorption and adjustable infrared radiation effects. Due to the effect of FP resonance, significant changes in emissivity within the infrared band can be achieved by changing the thickness of the ZnSe layer. Based on infrared thermal radiation at high and low temperatures, emissivity adjustment can reach 0.49. We then compare and analyze the red shift of peak wavelengths in the infrared range corresponding to changes in different layer thicknesses. Furthermore, the emission enhancement at the peak wavelength is analyzed through the electric field distribution. Additionally, the absorption of sunlight over a wide angular range and the radiative capability in the infrared spectrum are studied. Overall, our structure, while maintaining infrared radiation adjustability, has low absorption in the solar light band, making it more suitable for aerospace applications.

2. Structural Design and Analysis

To achieve aerospace applications in a space environment, the structure needs to dissipate heat radiatively at high temperatures while exhibiting weak energy dissipation at low temperatures. Furthermore, it needs to have low solar radiation absorption to achieve thermal stability of the device. Figure 1 illustrates the coating structure controlled by phase change materials for aerospace. In two different states corresponding to high and low temperatures, they exhibit partial reflection of visible light from the solar spectrum, at 0.41 and 0.26, respectively. Due to the material characteristics of the structure, they also have a certain degree of transparency to visible light (0.37 and 0.63), avoiding excessive heat accumulation caused by absorbing a large amount of solar radiation. Accordingly, Batista et al. observed the change in transmittance of VO₂ in the infrared band caused by state changes [27]. In the infrared band, when the spacecraft component structure faces the direct sunlight, the temperature is higher, resulting in a higher infrared emissivity. The coating structure allows it to radiate energy to the external environment, achieving radiative cooling. However, when the device is on the shadowed side, the temperature is lower, resulting in lower emissivity and thus less energy dissipation [28]. Overall, during the operation of the device in space, when in contact with the sun, the thermal regulation achieved through the thermochromic control of phase change materials enables the device to maintain thermal stability, thereby extending its operational lifespan.

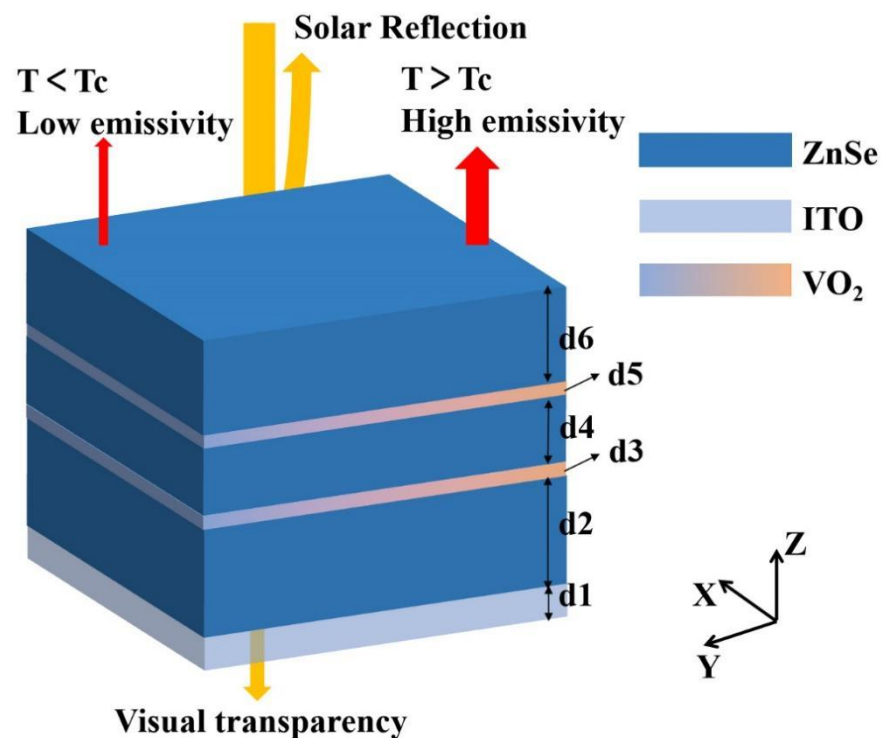


Figure 1. Schematic diagram of the designed intelligent thermal radiator.

To explore the optical performance of this structure, we used the commercial software Comsol (Comsol 2022) for finite element simulation. During the modeling process, a two-dimensional model was used, focusing solely on the depth of the structure with periodic boundary conditions. The spacecraft device coating structure we designed consists of the materials ITO, VO₂, and ZnSe. Owing to the dual states of VO₂, exhibiting metallic and dielectric properties, a multilayer film structure in the form of an FP configuration is typically designed to achieve modulation of the infrared emissivity. In the multilayer film structure we designed, to reduce the absorption within the solar spectrum range, the depth of the VO₂ layer was set as d₃ = d₅ = 0.03 μm. The optimized thickness of the top ZnSe

layer was 1.13 μm . According to Kirchhoff's law, at thermal equilibrium, the emissivity of a structure can be obtained from its absorptivity as [29–31]:

$$R_\lambda + \alpha_\lambda + T_\lambda = 1 \quad (1)$$

Therefore, the emissivity can be expressed as:

$$\varepsilon_\lambda = \alpha_\lambda = 1 - R_\lambda - T_\lambda \quad (2)$$

Based on the above relationship, where R_λ and T_λ represent the reflectance and transmittance of the structure, respectively, the emission of the object can be calculated as [32]:

$$\varepsilon = \frac{\int_{2.5}^{25} (1 - R) I_{BB}(\lambda, T) d\lambda}{\int_{2.5}^{25} I_{BB}(\lambda, T) d\lambda} \quad (3)$$

wherein, $I_{BB}(\lambda, T)$ is the blackbody radiation intensity. Therefore, according to Planck's blackbody radiation law, the average absorption in the solar spectrum segment is [33,34]:

$$\alpha = \frac{\int_{0.3}^{2.5} (1 - R) S(\lambda, T) d\lambda}{\int_{0.3}^{2.5} S(\lambda, T) d\lambda} \quad (4)$$

where $S(\lambda, T)$ represents the AM1.5 solar spectrum, with a spectral range of 0.3–2.5 μm . We can understand that within this range, approximately 50% of solar radiation is dependent on the visible light spectrum. Therefore, by comparing the absorption of the structure within the visible light range, we can roughly assess its absorption capability within the solar spectrum range.

Furthermore, for this simulation, the spectra are set within the wavelength ranges of 0.3–2.5 μm for solar light wavelength and 2.5–25 μm for infrared light wavelength. The optical data for the material ZnSe are sourced from reference [35]. As a thermochromic material, VO_2 exhibits abrupt changes in its optical properties due to temperature variations. In the low temperature dielectric phase of VO_2 , it can be represented using tensors as a uniaxial medium [36,37]:

$$\varepsilon_i(w) = \begin{pmatrix} \varepsilon_O(w) & 0 & 0 \\ 0 & \varepsilon_O(w) & 0 \\ 0 & 0 & \varepsilon_E(w) \end{pmatrix} \quad (5)$$

As can be seen, $\varepsilon_O(w)$ and $\varepsilon_E(w)$ correspond to the cases where the incident electric field is perpendicular and parallel to the optical axis, respectively. When the light incident is perpendicular to the axis, the material's dielectric constant can be represented as follows [38]:

$$\varepsilon(w) = \varepsilon_\infty + \sum_{i=1}^{N_L} \frac{S_i w_i^2}{w_i^2 - i\gamma_i w - w^2} \quad (6)$$

Regarding the above equation, S_i , i , γ_i , and w_i correspond to the phonon mode indices, the oscillation strength, the photon vibration frequency, and the damping factor, respectively.

As the temperature increases beyond the phase transition temperature, VO_2 transitions to a high-temperature metallic state. Its optical dielectric constant can be expressed as [39]:

$$\varepsilon_m(w) = -\varepsilon_\infty \frac{w_\Gamma^2}{w^2 - iw\gamma} \quad (7)$$

In the above equation, ε_∞ corresponds to the high frequency constant, and the plasma frequency and collision frequency are denoted by w_Γ and γ , respectively.

3. Results and Discussion

We first studied the effect of varying the thickness of two layers of ZnSe within the FP cavity structure on the infrared emission, as shown in Figure 2. It can be observed that the infrared emissivity of the structure undergoes significant changes before and after the thermotropic phase transition of the material VO₂. When the temperature is below the phase transition temperature, it can be seen that throughout the process of increasing d2 and d4 thicknesses, the corresponding emissivity remains relatively low. Specifically, as the thickness of d2 increases gradually, the emissivity generally shows a decreasing trend. However, as d4 increases gradually, it exhibits a trend of initially increasing and then decreasing when d2 is between 0.2 and 0.5 μm. When the temperature is above the phase transition temperature, it can be observed that throughout the process of increasing d2 and d4, the corresponding emissivity becomes relatively high. While the emissivity generally decreases as the thickness of d2 increases, it shows a trend of initially increasing and then decreasing when d4 increases gradually, particularly when d2 is between 0.2 and 1.0 μm. Therefore, within the infrared wavelength range, the bottom FP cavity exhibits weaker structural emission effects compared to the top FP cavity, and emission primarily depends on the FP cavity where d4 is located [40–45]. Then, through calculations, we obtained the results shown in Figure 2c, from which it can be inferred that within the selected range of variation, the difference in emission regulation capability is only 0.18. The intelligent thermal radiator aims to achieve the optimal emission regulation effect, and from the figure, it is determined that the optimal emission regulation capability occurs at d2 = 0.8 μm, d4 = 0.6 μm, where the emission regulation equals 0.49. Furthermore, to minimize the impact of solar radiation absorption on device thermal stability, we selected the material ZnSe, with high transparency in visible light, as the dielectric layer, and the material ITO as the infrared-range metal reflector. Additionally, it is noted that visible light absorption accounts for more than half of solar light absorption. Therefore, from the perspective of material properties, the absorption capacity of the material VO₂ before and after undergoing a thermally induced phase transition essentially represents solar radiation absorption. Observing Figure 3 reveals that the maximum solar absorption, reaching 0.33, occurs as the thickness of the two ZnSe layers varies under different temperature conditions. Among them, under the structural parameters determined by the optimal emission regulation, the corresponding solar absorption is only 0.3. In summary, the aerospace intelligent thermal radiator designed by us has a solar absorption of 0.3 and an emission regulation capability of 0.49, which promotes the application and development of aerospace devices to a certain extent [46].

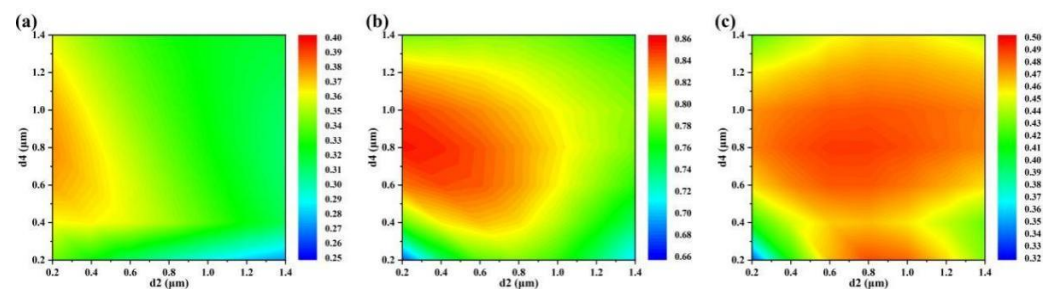


Figure 2. (a,b) The infrared emissivity at low and high temperatures, respectively, corresponding to variations in thicknesses d2 and d4. (c) The emissivity adjustment capability corresponding to variations in thicknesses d2 and d4.

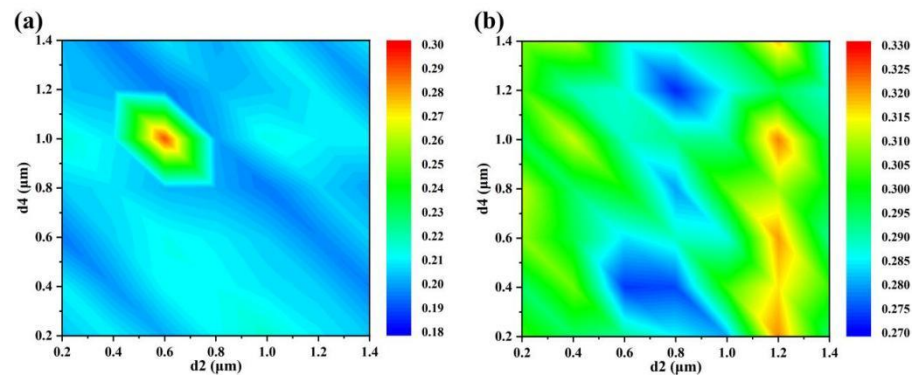


Figure 3. (a) The corresponding average solar band absorptance at low temperatures for varying thicknesses d_2 and d_4 . (b) The corresponding average solar band absorptance at high temperatures for varying thicknesses d_2 and d_4 .

To better understand the absorption and radiation performance under optimized structural parameters, the solar absorption and normalized AM1.5, as well as infrared emission and normalized blackbody radiation intensity of material VO_2 under different states before and after phase transition, were compared through simulation calculations, as shown in Figure 4. Figure 4a illustrates that the coating structure shows minimal absorption within the visible light spectrum range of solar radiation, regardless of whether they are in dielectric or metallic states. This feature contributes to the modest absorption of solar radiation [47–50]. However, within the infrared range, the dielectric state also exhibits some metallic properties, allowing it to form part of the FP cavity. Nevertheless, compared to the structure in the metallic state, the FP cavity formed by the dielectric state is relatively weaker. Consequently, the metallic state exhibits a stronger peak, as reflected in Figure 4b.

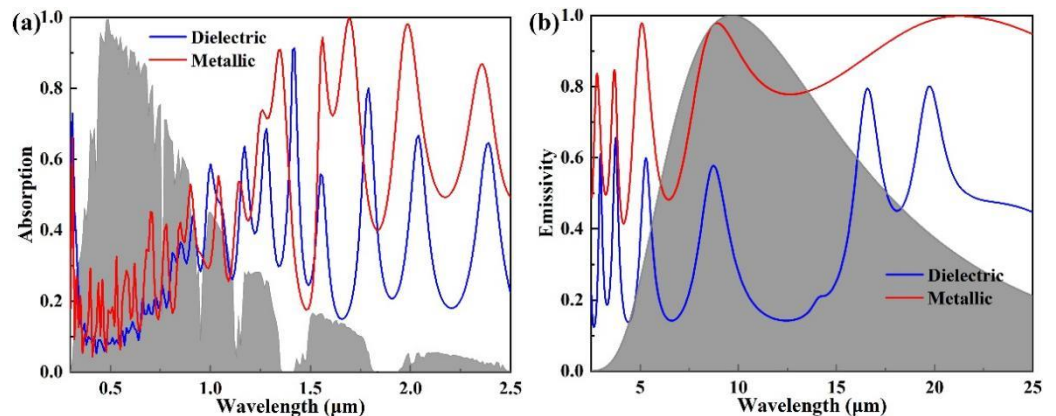


Figure 4. (a) The absorption of solar radiation by phase change materials in their dielectric and metallic states differs. (b) Infrared emission of structures in dielectric and metallic states of phase change material.

Table 1 compares our work with the previous literature in terms of structural design, solar absorption, and radiation management [22,51,52]. It is evident from this comparison that our designed structure outperforms in both solar absorption and radiation management, making it more conducive to the application of intelligent thermal control in space.

Table 1. Comparison with previous work on solar absorption and radiation regulation.

Reference	Structure Design	Solar Absorption	Radiation Regulation
[22]	VO ₂ /HfO ₂ /Al	-	0.51
[51]	VO ₂ /SiO ₂ /AZO/CaF ₂	0.3	0.26
[52]	VO ₂ /SiO ₂ /Ag	0.38	0.47
Our work	ZnSe(VO ₂ /ZnSe/VO ₂ /ZnSe)ITO	0.3	0.49

The ability to adjust infrared emission is crucial for designing intelligent aerospace thermal control devices [53–56]. To gain a deeper understanding of the role of the phase change material VO₂ in infrared emission modulation, we elucidate this phenomenon from the perspective of electric field distribution. Figure 5 illustrates the electric field distribution corresponding to the dielectric state and the metallic state of the intelligent aerospace radiator at 5.08 μm and 21.24 μm wavelengths. As depicted in Figure 5a,b, the electric field distribution is primarily concentrated in the dielectric material, with the majority absorbed by ZnSe. Similarly, due to the absorption of ZnSe material, the intelligent aerospace radiator exhibits significant emission capabilities at both the metallic and dielectric states at a 21.24 μm wavelength, with weaker absorption capabilities observed in the ZnSe material within the bottom layer of the FP cavity at this wavelength. VO₂ exhibits stronger metallic properties at high temperatures, whereas at low temperatures, it primarily exhibits dielectric properties, leading to stronger absorption capabilities in the FP cavity at high temperatures [57,58].

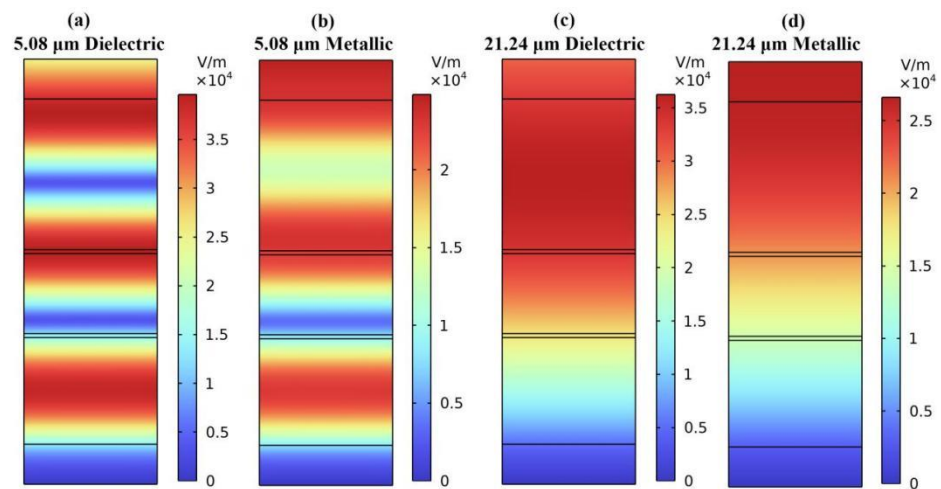


Figure 5. (a,b) The electric field distribution within the structures in dielectric and metallic states at a wavelength of 5.08 μm . (c,d) The electric field distribution within the structures in dielectric and metallic states at a wavelength of 21.24 μm .

The performance differences faced by aerospace thermal control devices under different angles as they continuously rotate in space is a major issue that needs to be studied [59,60]. In order to effectively expand the practical application of intelligent space radiators, we conducted simulation calculations to compute the spectral absorptance of the structure over a wide angle range. Figure 6 illustrates the spectral directional absorptance of the spacecraft intelligent radiator in both metallic and dielectric states across the solar spectrum range. As shown in Figure 6a,b, regardless of the state, the spectral directional absorptance of the spacecraft intelligent radiator exhibits multiple peaks at high angles of incidence. Additionally, with increasing angle of incidence, the peak wavelengths of spectral directional absorptance tend to blue-shift. Furthermore, the spectral directional absorptance maintains relatively low levels within a wide range of incident angles.

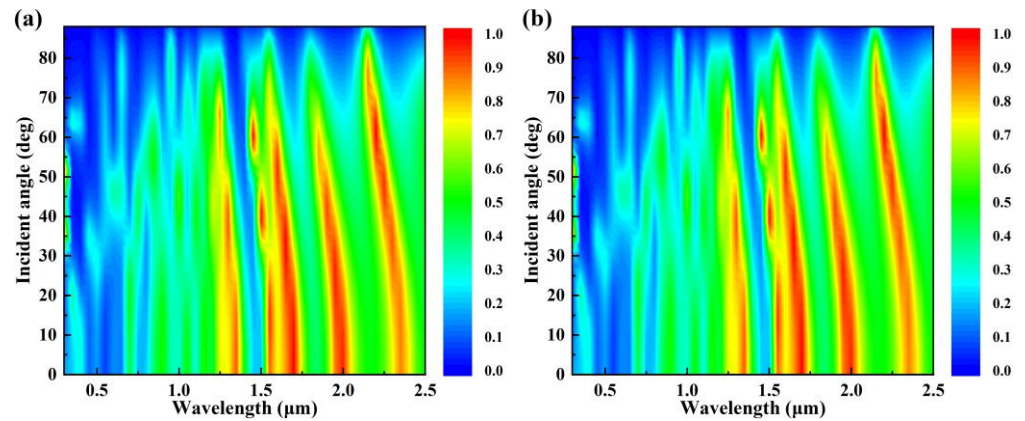


Figure 6. The absorptance corresponding to changes in the angle of incident within the solar band spectrum. (a) At high temperatures. (b) At low temperature.

Furthermore, by simulating the angular performance of the structural emission ability at different temperatures within the infrared spectral range, the independence of emission regulation was obtained, as shown in Figure 7. Overall, regardless of the state, the spectral directional radiance of the spacecraft intelligent radiator remains at relatively low levels at a larger incident angle. As observed in Figure 7a, when the incident angle is less than 60° , the spectral directional radiance of the spacecraft intelligent radiator under the metallic state exhibits only slight changes with increasing incident angles within the 5 to 30 μm spectral range, but significantly decreases when the incident angle exceeds 60° . As shown in Figure 7b, the spectral directional radiance of the spacecraft intelligent radiator under the dielectric state appears to be independent of the incident angle and maintains relatively low levels within the 2.5 to 25 μm spectral range. These results indicate that the device we designed has good thermal radiation performance within a certain angle range. This result has been applied in many fields [61–64].

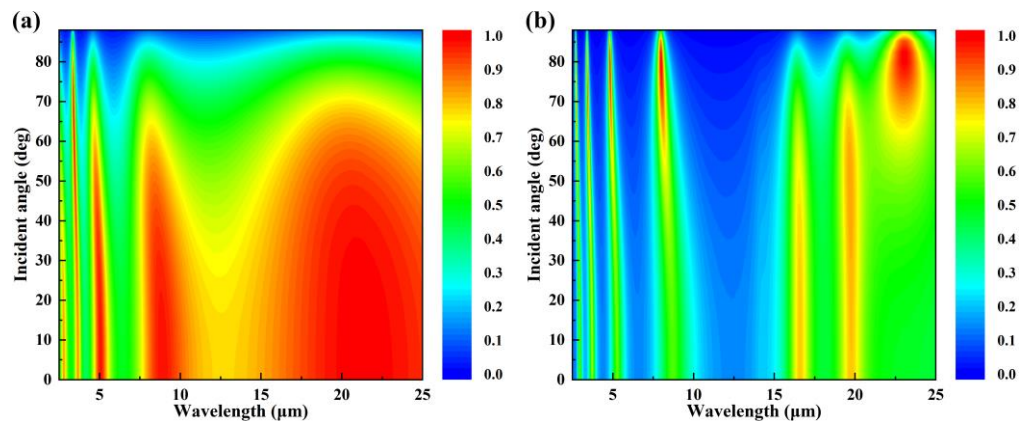


Figure 7. Emissivity corresponding to changes in the angle of incident within the infrared range. (a) At high temperatures. (b) At low temperature.

Figure 8 depicts the polarization-averaged total directional absorptance and total directional radiance of the spacecraft intelligent radiator under two states. Over a wide range of incident angles, the total directional absorptance is observed to remain at relatively low levels, as illustrated in Figure 8a. It is worth noting that, with increasing incident angles, there is a tendency for the total directional absorptance to rise, which can be ascribed to the blue shift observed in the peak wavelengths of spectral directional absorptance [65–67]. Concerning the total directional emission, as depicted in Figure 8b, its variation contrasts with the change observed in the total directional absorption rate as the incident angle increases. When the incident angle is less than 30° , the total directional radiation change of

the metallic state is small, while the total directional radiation change of the dielectric state is 45° and the change is small [68–70]. However, for incident angles greater than 45° , the total directional radiance significantly decreases with increasing incident angle.

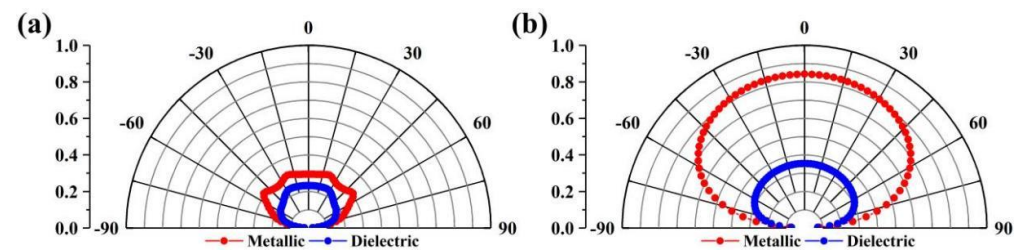


Figure 8. (a) The average absorption in the solar band spectrum corresponding to changes in the angle of incident. (b) The emission in the infrared range corresponding to changes in the angle of incident.

4. Conclusions

In summary, an intelligent radiative device based on the phase change material VO_2 and utilizing FP resonance has demonstrated outstanding performance in thermal control systems of spacecraft. By leveraging the tunable properties of VO_2 and optimizing layer thickness, we have achieved an emission tuning of 0.49 within the infrared range, while maintaining low absorption of solar radiation at 0.3. This enables effective heat dissipation in space environments while minimizing losses, ensuring stable internal temperatures of spacecraft components. The ability to adaptively adjust radiation characteristics enhances the performance of device equipment under different transient thermal environmental conditions, thereby improving the efficiency of spacecraft components. Meeting and adapting to large-angle performance and uncorrelated effects during solar rotation aids in refining spacecraft thermal management techniques and enhances reliability and efficiency in space exploration endeavors.

Author Contributions: Conceptualization, X.K., H.S., S.L. and Z.Y.; data curation, X.K., H.S. and N.G.; formal analysis, X.K. and Y.Y.; methodology, X.K., H.S., S.L., Z.Y., N.G. and Y.Y.; resources, X.K., H.S. and S.L.; software, N.G., Y.Y. and Z.Y.; data curation, X.K.; writing—original draft preparation, X.K.; writing—review and editing, S.L., Z.Y., N.G. and Y.Y. All authors have read and agreed to the published version of the manuscript.

Funding: The authors are grateful for the support of the National Natural Science Foundation of China (No. 51606158, 11604311, 12074151); the funding from the Scientific Research Fund of Sichuan Provincial Science and Technology Department (2020YJ0137; 2020YFG0467; 2021JDRC0019); the College Students' innovation and entrepreneurship training program (S202110619073; S202110619069) and; the undergraduate Innovation Fund Project of SWUST (CX 21-099; LX2020010; CX21-008).

Institutional Review Board Statement: Not applicable.

Informed Consent Statement: Not applicable.

Data Availability Statement: Publicly available datasets were analyzed in this study. This data can be found here: [<https://www.lumerical.com/>] (accessed on 1 January 2020).

Conflicts of Interest: The authors declare no conflicts of interest.

References

- Li, T.; Zhai, Y.; He, S.; Gan, W.; Wei, Z.; Heidarinejad, M.; Dalgo, D.; Mi, R.; Zhao, X.; Song, J.; et al. A radiative cooling structural material. *Science* **2019**, *364*, 760–763. [[CrossRef](#)] [[PubMed](#)]
- Liang, S.R.; Xu, F.; Li, W.X.; Yang, W.X.; Cheng, S.B.; Yang, H.; Chen, J.; Yi, Z.; Jiang, P.P. Tunable smart mid in-framed thermal control emitter based on phase change material VO_2 thin film. *Appl. Therm. Eng.* **2023**, *232*, 121074. [[CrossRef](#)]
- Zhang, F.C.; Camarero, P.; Haro-González, P.; Labrador-Páez, L.; Jaque, D. Optical trapping of optical nanoparticles: Fundamentals and applications. *Opto-Electron. Sci.* **2023**, *2*, 230019. [[CrossRef](#)]

4. Jaramillo-Fernandez, J.; Whitworth, G.L.; Pariente, J.A.; Blanco, A.; Garcia, P.D.; Lopez, C.; Sotomayor-Torres, C.M. A Self-Assembled 2D Thermofunctional Material for Radiative Cooling. *Small* **2019**, *15*, e1905290. [[CrossRef](#)] [[PubMed](#)]
5. Minin, I.V.; Minin, O.V.; Cao, Y.H.; Yan, B.; Wang, Z.B.; Luk'yanchuk, B. Photonic lenses with whispering gallery waves at Janus particles. *Opto-Electron. Sci.* **2022**, *1*, 210008. [[CrossRef](#)]
6. Raman, A.P.; Anoma, M.A.; Zhu, L.; Rephaeli, E.; Fan, S. Passive radiative cooling below ambient air temperature under direct sunlight. *Nature* **2014**, *515*, 540–544. [[CrossRef](#)] [[PubMed](#)]
7. Wang, S.; Jiang, T.; Meng, Y.; Yang, R.; Tan, G.; Long, Y. Scalable thermochromic smart windows with passive radiative cooling regulation. *Science* **2021**, *374*, 1501–1504. [[CrossRef](#)] [[PubMed](#)]
8. Watt, M.S.; Holdaway, A.; Watt, P.; Pearse, G.D.; Palmer, M.E.; Steer, B.S.C.; Camarretta, N.; McLay, E.; Fraser, S. Early Prediction of Regional Red Needle Cast Outbreaks Using Climatic Data Trends and Satellite-Derived Observations. *Remote Sens.* **2024**, *16*, 1401. [[CrossRef](#)]
9. Gigli, C.; Leo, G. All-dielectric $\chi(2)$ metasurfaces: Recent progress. *Opto-Electron. Adv.* **2022**, *5*, 210093. [[CrossRef](#)]
10. Yue, Z.; Li, J.T.; Li, J.; Zheng, C.L.; Liu, J.Y.; Lin, L.; Guo, L.; Liu, W. Terahertz metasurface zone plates with arbitrary polarizations to a fixed polarization conversion. *Opto-Electron. Sci.* **2022**, *1*, 210014. [[CrossRef](#)]
11. Li, W.X.; Liu, Y.H.; Ling, L.; Sheng, Z.X.; Cheng, S.B.; Yi, Z.; Wu, P.H.; Zeng, Q.D.; Tang, B.; Ahmad, S. The tunable absorber films of grating structure of AlCuFe quasicrystal with high Q and refractive index sensitivity. *Surf. Interfaces* **2024**, *48*, 104248. [[CrossRef](#)]
12. Zeng, C.; Lu, H.; Mao, D.; Du, Y.Q.; Hua, H.; Zhao, W.; Zhao, J. Graphene-empowered dynamic metasurfaces and metadevices. *Opto-Electron. Adv.* **2022**, *5*, 200098. [[CrossRef](#)]
13. Ma, J.; Wu, P.H.; Li, W.X.; Liang, S.R.; Shangguan, Q.Y.; Cheng, S.B.; Tian, Y.H.; Fu, J.Q.; Zhang, L.B. A five-peaks graphene absorber with multiple adjustable and high sensitivity in the far infrared band. *Diam. Relat. Mater.* **2023**, *136*, 109960. [[CrossRef](#)]
14. Xiong, H.; Suo, M.; Li, X.K.; Xiao, D.P.; Zhang, H.Q. Design of Energy-Selective Surface with Ultra-wide Shielding band for High-Power Microwave Protection. *ACS Appl. Electron. Mater.* **2024**, *6*, 696–701. [[CrossRef](#)]
15. Voti, R.L.; Larciprete, M.C.; Leahu, G.; Sibilia, C.; Bertolotti, M. Optimization of thermochromic VO₂ based structures with tunable thermal emissivity. *J. Appl. Phys.* **2012**, *112*, 034305. [[CrossRef](#)]
16. Yang, J.; Xu, Z.; Ye, H.; Xu, X.; Wu, X.; Wang, J. Performance analyses of building energy on phase transition processes of VO₂ windows with an improved model. *Appl. Energy* **2015**, *159*, 502–508. [[CrossRef](#)]
17. Gonçalves, A.; Resende, J.; Marques, A.; Pinto, J.; Nunes, D.; Marie, A.; Goncalves, R.; Pereira, L.; Martins, R.; Fortunato, E. Smart optically active VO₂ nanostructured layers applied in roof-type ceramic tiles for energy efficiency. *Sol. Energy Mater. Sol. Cells* **2016**, *150*, 1–9. [[CrossRef](#)]
18. Hendaoui, A.; Émond, N.; Dorval, S.; Chaker, M.; Haddad, E. VO₂-based smart coatings with improved emittance-switching properties for an energy-efficient near room-temperature thermal control of spacecrafts. *Sol. Energy Mater. Sol. Cells* **2013**, *117*, 494–498. [[CrossRef](#)]
19. Uday, K.C.; Nader, E. Modeling vanadium dioxide phase transition due to continuous-wave optical signals. *Opt. Express* **2015**, *23*, 445–451. [[CrossRef](#)]
20. Aziznezhad, M.; Goharshadi, E.K.; Mehrkhah, R.; Ghafurian, M.M. Alkaline earth metals doped VO₂ nanoparticles for enhanced interfacial solar steam generation. *Mater. Res. Bull.* **2022**, *149*, 111705. [[CrossRef](#)]
21. Kruzelecky, R.V.; Haddad, E.; Jamroz, W.; Soltani, M.; Chaker, M.; Colangelo, G. Thinfilm smart radiator tiles with dynamically tuneable thermal emittance. *SAE Technol.* **2005**, *1*, 2096.
22. Guan, H.; Ren, F.F.; Liang, S.H.; Gu, J.X.; Geng, C.C.; Wei, H.; Dou, S.L.; Zhao, J.P.; Li, Y. Ultra-High Transmission Broadband Tunable VO₂ Optical Limiter. *Laser Photonics Rev.* **2023**, *17*, 2200653. [[CrossRef](#)]
23. Araki, K.; Zhang, R.Z. Simultaneous solar rejection and infrared emission switching using an integrated dielectrics-on-VO₂ metasurface. *AIP Adv.* **2022**, *12*, 055205. [[CrossRef](#)]
24. Nelson, A.M.; Sanjuan, J.; Guzmán, F. 1/f Noise Mitigation in an Opto-Mechanical Sensor with a Fabry–Pérot Interferometer. *Sensors* **2024**, *24*, 1969. [[CrossRef](#)] [[PubMed](#)]
25. Li, W.X.; Liu, M.S.; Cheng, S.B.; Zhang, H.F.; Yang, W.X.; Yi, Z.; Zeng, Q.D.; Tang, B.; Ahmad, S.; Sun, T.Y. Polarization independent tunable bandwidth absorber based on single-layer graphene. *Diam. Relat. Mater.* **2024**, *142*, 110793. [[CrossRef](#)]
26. Buono, W.T.; Forbes, A. Nonlinear optics with structured light. *Opto-Electron. Adv.* **2022**, *5*, 210174. [[CrossRef](#)]
27. Batista, C.; Mendes, J.; Teixeira, V.; Carneiro, J. Reactive DC magnetron sputtering of vanadium oxide thin films. *Mater. Sci. Forum* **2008**, *587*, 343–347. [[CrossRef](#)]
28. Zhang, T.X.; Tao, C.; Ge, S.X.; Pan, D.W.; Li, B.; Huang, W.X.; Wang, W.; Chu, L.Y. Interfaces coupling deformation mechanisms of liquid-liquid-liquid three-phase flow in a confined microchannel. *Chem. Eng. J.* **2022**, *434*, 134769. [[CrossRef](#)]
29. Park, Y.; Asadchy, V.S.; Zhao, B.; Guo, C.; Wang, J.; Fan, S. Violating Kirchhoff's Law of Thermal Radiation in Semitransparent Structures. *ACS Photonics* **2021**, *8*, 2417–2424. [[CrossRef](#)]
30. Liang, S.; Xu, F.; Yang, H.; Cheng, S.; Yang, W.; Yi, Z.; Song, Q.; Wu, P.; Chen, J.; Tang, C. Ultra long infrared metamaterial absorber with high absorption and broad band based on nano cross surrounding. *Opt. Laser Technol.* **2023**, *158*, 108789. [[CrossRef](#)]
31. Krasikov, S.; Tranter, A.; Bogdanov, A.; Kivshar, Y. Intelligent metaphotonics empowered by machine learning. *Opto-Electron. Adv.* **2022**, *5*, 210147. [[CrossRef](#)]

32. Luo, J. Dynamical behavior analysis and soliton solutions of the generalized Whitham–Broer–Kaup–Boussineq–Kupershmidt equations. *Results Phys.* **2024**, *60*, 107667. [[CrossRef](#)]
33. Zhang, Y.; Pu, M.; Jin, J.; Lu, X.; Guo, Y.; Cai, J.; Zhang, F.; Ha, Y.; He, Q.; Xu, M.; et al. Crosstalk-free achromatic full Stokes imaging polarimetry metasurface enabled by polarization-dependent phase optimization. *Opto-Electron. Adv.* **2022**, *5*, 220058. [[CrossRef](#)]
34. Chen, H.; Huang, Y.H.; Yu, L.; Li, Z.L.; Wang, G.; Dai, B.; Wang, Y. Ca₃Co₄O₉-based transverse thermoelectric heat flux sensors with high sensitivity and fast response time. *Appl. Phys. Lett.* **2024**, *124*, 013905. [[CrossRef](#)]
35. Querry, M.R. *Optical Constants of Minerals and Other Materials from the Millimeter to the Ultraviolet*; University of Missouri-Kansas City: Kansas City, MO, USA, 1987.
36. Yang, Q.; Xiong, H.; Deng, J.H.; Wang, B.X.; Peng, W.X.; Zhang, H.Q. Polarization-insensitive composite gradient-index metasurface array for microwave power reception. *Appl. Phys. Lett.* **2023**, *122*, 253901. [[CrossRef](#)]
37. Tang, C.J.; Nie, Q.M.; Cai, P.G.; Liu, F.X.; Gu, P.; Yan, Z.D.; Huang, Z.; Zhu, M.W. Ultra-broadband near-infrared absorption enhancement of monolayer graphene by multiple-resonator approach. *Diam. Relat. Mater.* **2024**, *141*, 110607. [[CrossRef](#)]
38. Leng, Q.; Su, H.H.; Liu, J.Q.; Zhou, L.; Qin, K.; Wang, Q.J.; Fu, J.Q.; Wu, S.; Zhang, X.J. Enhanced second-harmonic generation in monolayer MoS₂ on suspended metallic nanostructures by plasmonic resonances. *Nanophotonics* **2021**, *10*, 1871–1877. [[CrossRef](#)]
39. Meng, C.; Shui, T.; Yang, W.X. Coherent transfer of optical vortices via backward four-wave mixing in a double- Λ atomic system. *Phys. Rev. A* **2023**, *107*, 053712. [[CrossRef](#)]
40. Ayaz, R.M.A.; Balazadeh Koucheh, A.; Sendur, K. Broadband-Tunable Vanadium Dioxide (VO₂)-Based Linear Optical Cavity Sensor. *Nanomaterials* **2024**, *14*, 328. [[CrossRef](#)]
41. Li, W.X.; Zhao, W.C.; Cheng, S.B.; Yang, W.X.; Yi, Z.; Li, G.F.; Zeng, L.C.; Li, H.L.; Wu, P.H.; Cai, S.S. Terahertz Selective Active Electromagnetic Absorption Film Based on Single-Layer Graphene. *Surf. Interfaces* **2023**, *40*, 103042. [[CrossRef](#)]
42. Okamoto, K.; Tanaka, D.; Matsuyama, T.; Wada, K.; Arima, Y.; Tamada, K. Design and Optimization of Silver Nanostructured Arrays in Plasmonic Metamaterials for Sensitive Imaging Applications. *Photonics* **2024**, *11*, 292. [[CrossRef](#)]
43. Tsuji, K.; Ishikawa, T.; Memura, K.; Kawasaki, Y.; Iwaguchi, S.; Shimizu, R.; Ando, M.; Kawamura, S. Significance of Fabry-Perot Cavities for Space Gravitational Wave Antenna DECIGO. *Galaxies* **2024**, *12*, 13. [[CrossRef](#)]
44. Zhou, W.; Qin, X.; Lv, M.; Qiu, L.; Chen, Z.; Zhang, F. Design of a New Type of In-Hole Gold-Coated High-Performance Quasi-PCF Sensor Enhanced with Surface Plasmon Resonance. *Coatings* **2023**, *13*, 1261. [[CrossRef](#)]
45. Zhou, Z.; Liu, W.; Huang, H.; Ding, X.; Li, X. Enhancement of Photoelectric Performance Based on Ultrathin Wide Spectrum Solar Absorption in Cruciform Microstructure Germanium Solar Cells. *Coatings* **2023**, *13*, 1123. [[CrossRef](#)]
46. Zhou, S.; Bi, K.; Li, Q.; Mei, L.; Niu, Y.; Fu, W.; Han, S.; Zhang, S.; Mu, J.; Tan, L.; et al. Patterned Graphene-Based Metamaterials for Terahertz Wave Absorption. *Coatings* **2023**, *13*, 59. [[CrossRef](#)]
47. Xiong, H.; Ma, X.D.; Liu, H.S.; Xiao, D.Q.; Zhang, H.Q. Research on electromagnetic energy absorption and conversion device with four-ring multi-resistance structure. *Appl. Phys. Lett.* **2023**, *123*, 153902. [[CrossRef](#)]
48. Ha, Y.L.; Luo, Y.; Pu, M.B.; Zhang, F.; He, Q.; Jin, J.; Xu, M.; Guo, Y.; Li, X.; Li, X.; et al. Physics-data-driven intelligent optimization for large-aperture metalenses. *Opto-Electron. Adv.* **2023**, *6*, 230133. [[CrossRef](#)]
49. Serpetzoglou, E.; Konidakis, I.; Kourmoulakis, G.; Demeridou, I.; Chatzimanolis, K.; Zervos, C.; Kioseoglou, G.; Kymakis, E.; Stratakis, E. Charge carrier dynamics in different crystal phases of CH₃NH₃PbI₃ perovskite. *Opto-Electron. Sci.* **2022**, *1*, 210005. [[CrossRef](#)]
50. Tao, G.; Yi, Y.; Zang, M.; Zheng, Z.; Yi, Y. Simulated Performance of a Broadband Solar Absorber Composed of Sectioned Au Disk Structures and ZnS/Au Thin Layers. *Coatings* **2022**, *12*, 1863. [[CrossRef](#)]
51. Sun, K.; Xiao, W.; Wheeler, C.; Simeoni, M.; Urbani, A.; Gaspari, M.; Mengali, S.; de Groot, C.; Muskens, O.L. VO₂ metasurface smart thermal emitter with high visual transparency for passive radiative cooling regulation in space and terrestrial applications. *Nanophotonics* **2022**, *11*, 4101–4114. [[CrossRef](#)]
52. Zhang, D.; Wu, B.; Liu, H.; Yang, B.; Sun, Y.; Wu, X. Spacecraft smart radiation device with variable emission and low absorption based on phase change material VO₂. *Int. J. Therm. Sci.* **2023**, *185*, 108039. [[CrossRef](#)]
53. Bahrami, A.; Soltanifar, F.; Fallahi, P.; Meschi, S.S.; Sohani, A. Energy and Economic Advantages of Using Solar Stills for Renewable Energy-Based Multi-Generation of Power and Hydrogen for Residential Buildings. *Buildings* **2024**, *14*, 1041. [[CrossRef](#)]
54. Shanguan, Q.; Zhao, Y.; Song, Z.; Wang, J.; Yang, H.; Chen, J.; Liu, C.; Cheng, S.; Yang, W.; Yi, Z. High sensitivity active adjustable graphene absorber for refractive index sensing applications. *Diam. Relat. Mater.* **2022**, *128*, 109273. [[CrossRef](#)]
55. Chernomyrdin, N.V.; Musina, G.R.; Nikitin, P.V.; Dolganova, I.N.; Kucheryavenko, A.S.; Alekseeva, A.I.; Wang, Y.; Xu, D.; Shi, Q.; Tuchin, V.V.; et al. Terahertz technology in intraoperative neurodiagnostics: A review. *Opto-Electron. Adv.* **2023**, *6*, 220071. [[CrossRef](#)]
56. Ma, X.; Song, R.; Fan, Z.; Zhou, S. Phase-Change Metasurface by U-Shaped Atoms for Photonic Switch with High Contrast Ratio. *Coatings* **2021**, *11*, 1499. [[CrossRef](#)]
57. Feng, S.N.A.; Wang, Y.J.; Fei, S.R.; Yan, Z.D.; Yu, L.L.; Chen, J.; Tang, C.J.; Liu, F.X. Dual ultrahigh-Q Fano Resonances of 3D gap metamaterials for slow light from ultraviolet to visible range. *Opt. Commun.* **2023**, *549*, 129811. [[CrossRef](#)]
58. Li, Y.; Huang, X.J.; Liu, S.X.; Liang, H.W.; Ling, Y.Y.; Su, Y. Metasurfaces for near-eye display applications. *Opto-Electron. Sci.* **2023**, *2*, 230025. [[CrossRef](#)]

59. Li, W.; Yi, Y.; Yang, H.; Cheng, S.; Yang, W.X.; Zhang, H.; Yi, Z.; Yi, Y.; Li, H. Active Tunable Terahertz Bandwidth Absorber Based on single layer Graphene. *Commun. Theor. Phys.* **2023**, *75*, 045503. [[CrossRef](#)]
60. Huang, L.; Liu, J.Q.; Deng, H.M.; Wu, S. Phonon-like plasmonic resonances in a finitely long graphene nanoribbons array. *Adv. Opt. Mater.* **2018**, *6*, 1701378. [[CrossRef](#)]
61. Shangguan, Q.; Chen, Z.; Yang, H.; Cheng, S.; Yang, W.; Yi, Z.; Wu, X.; Wang, S.; Yi, Y.; Wu, P. Design of Ultra-Narrow Band Graphene Refractive Index Sensor. *Sensors* **2022**, *22*, 6483. [[CrossRef](#)]
62. Deng, X.; Shui, T.; Zhang, T.; Song, Y.; Yang, W.X. Coherent control of double-ring perfect optical vortex via hyper-Raman scattering in a Landau-quantized graphene. *Eur. Phys. J. Plus* **2023**, *138*, 737. [[CrossRef](#)]
63. Chowdhury, H.R.; Han, M. Fiber Optic Temperature Sensor System Using Air-Filled Fabry–Pérot Cavity with Variable Pressure. *Sensors* **2023**, *23*, 3302. [[CrossRef](#)] [[PubMed](#)]
64. Zhang, Y.; Yi, Y.; Li, W.; Liang, S.; Ma, J.; Cheng, S.; Yang, W.; Yi, Y. High Absorptivity and Ultra-Wideband Solar Absorber Based on Ti-Al₂O₃ Cross Elliptical Disk Arrays. *Coatings* **2023**, *13*, 531. [[CrossRef](#)]
65. Wu, Y.F.; Nie, Q.M.; Tang, C.J.; Yan, B.; Liu, F.X.; Zhu, M.W. Bandwidth tunability of graphene absorption enhancement by hybridization of delocalized surface plasmon polaritons and localized magnetic plasmons. *Discov. Nano* **2024**, *19*, 19. [[CrossRef](#)]
66. Li, W.; Ma, J.; Zhang, H.; Cheng, S.; Yang, W.; Yi, Z.; Yang, H.; Zhang, J.; Wu, X.; Wu, P. Tunable broadband absorber based on a layered resonant structure with a Dirac semimetal. *Phys. Chem. Chem. Phys.* **2023**, *25*, 8489–8496. [[CrossRef](#)]
67. Baeva, M.; Gets, D.; Polushkin, A.; Vorobyov, A.; Goltaev, A.; Neplokh, V.; Mozharov, A.; Krasnikov, D.V.; Nasibulin, A.G.; Mukhin, I.; et al. ITO-free silicon-integrated perovskite electrochemical cell for light-emission and light-detection. *Opto-Electron. Adv.* **2023**, *6*, 220154. [[CrossRef](#)]
68. Shangguan, Q.; Chen, H.; Yang, H.; Liang, S.; Zhang, Y.; Cheng, S.; Yang, W.; Yi, Z.; Luo, Y.; Wu, P. A “belfry-typed” narrow-band tunable perfect absorber based on graphene and the application potential research. *Diam. Relat. Mater.* **2022**, *125*, 108973. [[CrossRef](#)]
69. Koo, J.H.; Yun, H.W.; Lee, W.C.; Sunwoo, S.H.; Shim, H.J.; Kim, D.-H. Recent advances in soft electronic materials for intrinsically stretchable optoelectronic systems. *Opto-Electron. Adv.* **2022**, *5*, 210131. [[CrossRef](#)]
70. Barker, A.S.; Verleur, H.W.; Guggenheim, H.J. Infrared Optical Properties of Vanadium Dioxide Above and Below the Transition Temperature. *Phys. Rev. Lett.* **1966**, *17*, 1286. [[CrossRef](#)]

Disclaimer/Publisher’s Note: The statements, opinions and data contained in all publications are solely those of the individual author(s) and contributor(s) and not of MDPI and/or the editor(s). MDPI and/or the editor(s) disclaim responsibility for any injury to people or property resulting from any ideas, methods, instructions or products referred to in the content.